Strain-driven antiferromagnetic exchange interaction in $SrMnO_3$ probed by phase-shifted spin Hall magnetoresistance

J. J. L. van Rijn [1,*] D. Wang [2] B. Sanyal [2] and T. Banerjee [1,†]
[1]*University of Groningen, Zernike Institute for Advanced Materials, 9747 AG Groningen, The Netherlands*
[2]*Department of Physics and Astronomy, Uppsala University, Box-516, 75120 Uppsala, Sweden*

(Received 19 July 2022; revised 16 November 2022; accepted 17 November 2022; published 15 December 2022)

Multiferroics have found renewed interest in topological magnetism and for logic-in-memory applications. Among them, $SrMnO_3$, possessing strong magnetoelectric coupling, is gaining attention for the design of coexisting magnetic and polar orders upon straining. Here we demonstrate antiferromagnetic exchange interactions in strained SMO thin films extracted from a new feature in the phase response of spin Hall magnetoresistance, which has not been explored in earlier works, such as in magnetic insulators. We explain our findings with a model that incorporates magnetic anisotropy along the [110] direction, corroborates with density functional theory studies, and is consistent with the direction of ferroelectric polarization in $SrMnO_3$. The fundamental insights obtained from our studies establishes the potential of this material in magnetoelectrically coupled devices for different logic and memory applications.

DOI: 10.1103/PhysRevB.106.214415

I. INTRODUCTION

The ability to design, stabilize, and tune diverse order parameters in the same material system renders complex oxides useful for the study of emerging properties, relevant for alternative computing strategies [1–3]. In this respect, multiferroic materials, due to their simultaneous coupling between charge and magnetic order, enables electric field control of magnetization and spin transport, offering new prospects for low power memory, logic, or logic in memory applications. Less investigated is the antiferromagnetic order, intrinsic to such multiferroics, primarily due to it being unresponsive to modest magnetic fields. These studies are important not only for developing antiferromagnetic spintronics and topological magnetism, but also for unraveling the full potential of magnetoelectric coupling in these materials by stimulating different routes to tailor diverse magnetic order. This can be realized in multiferroic materials of complex oxides by modulating the strain, crystal structure, and oxygen defects.

The rare earth manganite $SrMnO_3$ (SMO) is a magnetic insulator and a G-type antiferromagnet with the magnetic and ferroelectric order linked to the same B-site Mn cation, resulting in a strong magnetoelectric coupling. From first-principles studies, a temperature- and strain-dependent phase diagram was recently established for SMO, highlighting the tunability of the magnetoelectric coupling with strain [4,5]. At strains above 1.6%, a ferroelectric phase with a substantial polarization is predicted due to orbital reordering and cation displacement, persisting up to room temperature for higher strains [4–7]. At coinciding polar and magnetic ordering temperatures, SMO promises sizable magnetoelectric coupling [4], making it an appealing material for applications.

Experimentally, the polar character in strained SMO films has been studied recently using various charge-mediated experimental techniques [8–13]. However, probing the antiferromagnetic order in similarly strained SMO thin films has proved to be challenging due to the coexistence of competing magnetic phases. This is compounded by the fact that fabrication of stoichiometric strained SMO thin films is nontrivial due to the formation of oxygen vacancies, which relaxes the strain [14–17]. For oxygen-deficient films, the manganese 4^+ oxidation state is reduced by the absence of negative oxygen atoms, promoting double exchange interaction and a ferromagnetic order.

Here we show how a new feature in the phase response of the spin Hall magnetoresistance (SMR), hitherto unreported, in tensile strained SMO thin films is explained by considering a coexistence of different antiferromagnetic domains, governed by magnetocrystalline anisotropy in SMO and complemented by bulk magnetization studies. The magnetic order is probed by analyzing both the phase and amplitude of the longitudinal SMR oscillations. SMR studies on SMO, until now, were found to be consistent with a ferromagnetic order attributed to oxygen-deficient SMO phases [18].

To understand different magnetic interactions that coexist in our strained SMO thin films, density functional theory (DFT) studies are performed both for stoichiometric and oxygen-deficient SMO, revealing remarkably large bond angle modulations, close to the film surface. We develop a model that incorporates magnetic anisotropy along the [110] direction, determined from the rotational dependence of the SMR, corroborated by DFT studies, and aligning well with recently predicted [4,5] ferroelectric polarization along the same direction in SMO.

*Corresponding author: j.j.l.van.rijn@rug.nl
†Corresponding author: t.banerjee@rug.nl

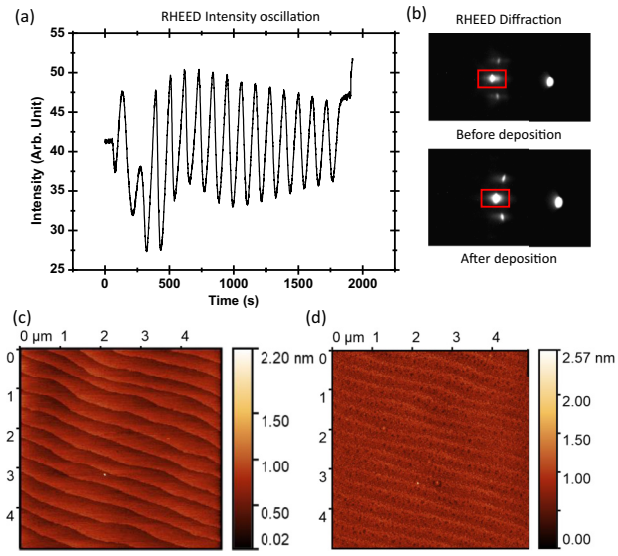

FIG. 1. In (a), *in situ* reflective high energy electron diffraction intensity oscillations are displayed. The oscillations indicate clear layer-by-layer growth, and from this a film thickness of 15 u.c. is determined. The diffraction spot used to obtain the intensity oscillations are shown in (b), marked with a red square. The AFM images of a STO (001) substrate (c) and SMO film in (d) both display a low roughness, which indicates the atomically flat surface. The STO terrace structure is clearly visible in (d).

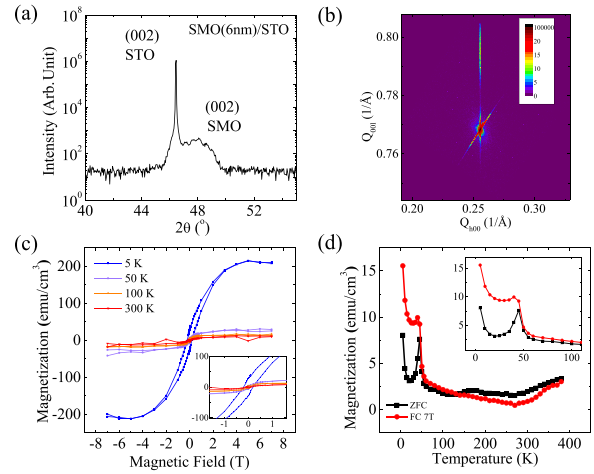

FIG. 2. The (002) SMO peak in (a) obtained from x-ray diffraction corresponds to −0.6% strain. From the reciprocal space mapping in (b), a fully epitaxial strain of 2.6% is confirmed. Magnetization vs temperature (*M*-*T*) for zero-field-cooled (ZFC) and field-cooled (FC) measurements is shown in (c). A measurement field of 1 kOe was applied during warming along the [100] crystallographic direction. In (d), the field-dependent magnetization (*M*-*H*) complements the (*M*-*T*), displaying a ferromagnetic loop only for 5 K. In the insets a zoom of the respective measurement curve is shown.

II. FILM GROWTH AND CHARACTERIZATION

$SrTiO_3$ (001) substrates are prepared by a standard protocol to obtain a TiO_2 terminated surface [19]. A topographic atomic force microscopy (AFM) image of a terminated substrate is shown in Fig. 1(c), indicating the terrace structure with a miscut of 0.05°. The surface roughness, calculated over the full scan, has a rms of 0.131 nm, indicating an atomically flat surface. The $SrMnO_3$ (SMO) thin films are grown by pulsed laser deposition at a substrate temperature of 800 °C and an oxygen pressure of 0.05 mbar using a KrF laser with a laser fluence of 2 J cm^{-2}. The films are postannealed at 600 °C for 30 min at an oxygen pressure of approximately 150 mbar. The surface structure of the SMO films is monitored using *in situ* reflective high-energy electron diffraction (RHEED) (Fig. 1). From the RHEED intensity oscillations we confirm layer-by-layer growth and ascertain the thickness of 15 u.c. The SMO film surface roughness of 0.145 nm, see Fig. 1(d), is comparable to the pristine substrate before growth, confirming the high quality of the films.

Using a four-axis cradle (Cu Kα, $\lambda = 1.54$) PANalytical x-ray diffractometer, 2θ diffraction spectra are recorded at room temperature, shown in Fig. 2. From the 2θ SMO peaks a fully strained perovskite SMO structure is confirmed, with an out-of-plane and in-plane strain of–0.6% and 2.6%, respectively.

To understand the impact of the oxygen vacancies on the magnetic order in SMO, bulk magnetization measurements are utilized. Using a Quantum Design superconducting quantum interference device (SQUID) magnetometer, in-plane magnetization loops are obtained for temperatures ranging from 5 to 300 K, displayed in Fig. 2(c). At 5 K, a tiny loop opening in *M*-*H* is observed and interpreted to arise from vacancy-driven weakening of the antiferromagnetic order. A net magnetization is observed between 5 and 50 K from the finite difference of magnetization measured for the zero-field-cooled curve and field-cooled curve shown in Fig. 2(d). Above 50 K, both curves meet and the magnetization decreases further and disappears at higher temperature.

III. COMPUTATIONAL DETAILS

Our simulations are based on first-principles electronic structure calculations within DFT. We first performed geometry optimization for the structure with fixed bottom two layers by employing the projector augmented wave (PAW) [20,21]–based density functional code VASP [22]. The plane-wave energy cutoff was set to 520 eV, and the force on each atom is converged to 0.01 eV/Å. The *k* integration in the Brillouin zone was performed using $7 \times 7 \times 1$ points for geometry optimization and $12 \times 12 \times 1$ points for self-consistent calculations. The optimized structure was then used as an input for the calculation of interatomic exchange parameters (J_{ij}) by means of the magnetic force theorem (MFT) [23] using the full-potential linear muffin-tin orbital (FP-LMTO) code RSPT [24]. To describe the exchange-correlation effects, we used the generalized gradient approximation (GGA) in the form of Perdew, Burke, and Ernzerhof (PBE) [25] augmented by the Hubbard-U corrections (PBE+U) [26,27]. The Coulomb U and intra-atomic Hund's exchange parameter *J* are added on Mn-*d* electrons as 2.7 and 1 eV, respectively, which have proven to be good values for Mn-based oxides [6,7]. Finally, we used the extracted J_{ij} and magnetocrystalline anisotropy energies (MAEs) to calculate the magnetic ordering temperature using classical Monte Carlo (MC)

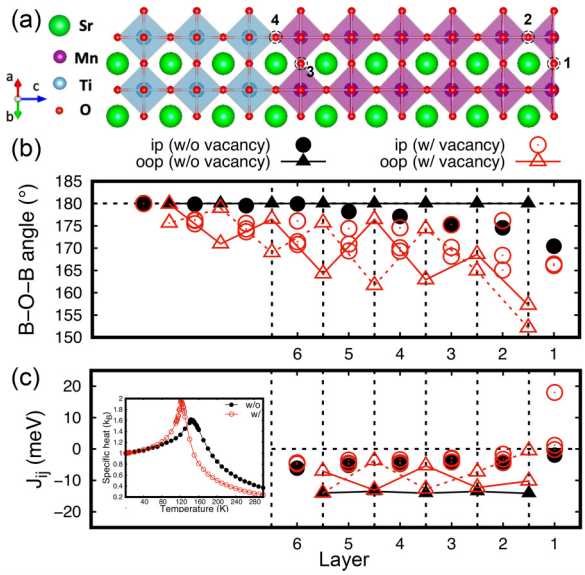

FIG. 3. (a) The side view of $SrMnO_3/SrTiO_3$ used in DFT+U calculations. Green, purple, cyan, and red balls represent Sr, Mn, Ti, and O atoms, respectively. The shaded areas indicate TiO_6 and MnO_6 octahedra. Dashed circles indicate the positions of oxygen vacancy. (b) The Mn-O-Mn bond angles and (c) the nearest-neighbor magnetic exchange parameters for structures with (filled circle and triangle) and without (empty circle and triangle) oxygen vacancy. Circle and triangle represent Mn-Mn pair in- (ip) and out-of-plane (oop) MnO_2 plane. In order to distinguish two different spin chains along the z direction, empty triangles are connected by solid and dashed lines. Vertical dashed lines are used to separate the MnO_2 layers. Positive and negative values of J_{ij} in (c) indicate FM and AFM coupling, respectively. The inset in (c) is the specific heat as a function of temperature obtained from Monte Carlo simulations. In (b) and (c), the MnO_2 layers are indicated by numbers with the surface (interface with STO) marked by 1(6).

simulations for the solution of the following spin Hamiltonian:

$$H = \sum_{i,j} J_{ij} e_i \cdot e_j - \sum_i K_i \left(\hat{e}_i \cdot e_i^K\right)^2,$$

which is implemented in the Uppsala atomistic spin dynamics (UPPASD) code [28]. For this purpose, a $70 \times 70 \times 1$ cell (58 800 atoms) was considered. The transition state barriers are obtained by using the climbing image nudged elastic band (cNEB) method [29,30].

The structural model considered in this paper consists of six layers of SMO on top of three STO layers in the unit cell [Fig. 3(a)] with the vacuum region set to 20 Å. Since the theoretically obtained equilibrium lattice parameters of bulk SMO and bulk STO are 3.945 and 3.836 Å, we fix the in-plane lattice parameter of the structural model as 3.945 Å, which matches closely with the equilibrium lattice parameters of bulk SMO and STO and corresponds well with the experimental lattice mismatch of 2.9%. In order to simulate structures with different magnetic configurations, such as ferromagnetic (FM) and three antiferromagnetic (AFM), A-type, C-type, and G-type, a $\sqrt{2} \times \sqrt{2}$ in-plane supercell is chosen.

TABLE I. Calculated relative energies of structures with oxygen vacancy. The ground-state energy is set to zero. Numbers in parenthesis are the oxygen vacancy formation energies. They are calculated by E_{form}=$E_{w/}$-$E_{w/o}$-E_{oxygen}, unit in eV.

	Site 1	Site 2	Site 3	Site 4
A-type	0.19(0.01)	0.74(0.56)	1.14(0.96)	2.09(1.91)
C-type	0.19(0.04)	0.73(0.58)	1.62(1.47)	2.33(2.18)
G-type	0.00(0.02)	1.13(1.15)	1.54(1.56)	2.43(2.45)
FM	0.16(−0.41)	1.07(0.50)	1.09(0.52)	2.42(1.86)

IV. RESULTS AND DISCUSSION

Unlike bulk SMO, there are some interesting features for strained thin films on a substrate, linked to the Mn-O-Mn bond angles, that are essential to the understanding of the exchange mechanism and the exchange parameters. The in-plane Mn-O-Mn angle, as shown by filled circles in Fig. 3(b), gradually decreases from 180° (the sixth layer) to 170° (the surface layer), which directly leads to the consequence in Fig. 3(c) that the AFM coupling changes from –6.10 to–1.97 meV. This follows from the Goodenough-Kanamori-Anderson (GKA) rule that the AFM exchange is weakened by reducing the Mn-O-Mn angle from 180°. On the other hand, all the out-of-plane angles keep the same value as the bulk SMO (180°). Therefore the exchange parameters remain almost unchanged [as shown in Fig. 3(c) with the black triangles]. Further, we find the magnitude of the out-of-plane exchange parameter is, in general, larger than the in-plane exchange parameters. This is because the nearest Mn-Mn distances parallel and perpendicular to the interface are different due to the tensile strain introduced by the STO substrate. The averaged c/a ratio of the SMO thin film amounts to 0.96 from geometry optimization.

Due to the tensile strain introduced by the STO substrate and depending on the growth conditions of the thin films, oxygen vacancies tend to be the dominant type of defect in this material. In our DFT simulations, we created oxygen vacancies at four different sites [see Fig. 3(a)] and performed geometry optimization for each structure. Results are shown in Table I. First, as shown in the first column (site 1), regardless of the magnetic configuration, the oxygen vacancy tends to be at the surface layer. Second, the ground-state structure is G-type AFM with the oxygen vacancy at the surface layer. Third, the energy of the structure with oxygen at the MnO_2 layer (sites 1 and 3) is much smaller than the case on the TiO layer (sites 2 and 4). In order to estimate the energy involved in the diffusion of oxygen vacancy from one layer to another, we performed nudged elastic band (NEB) calculations. They correspond to the vacancy transition from the top layer (site 1) to the layer below (site 2) and also from the six layer (site 3) to the interface (site 4). The transition barriers are 1.9 and 3.2 eV, respectively. This indicates that the vacancy is easy to move when close to the surface, while it is hard when present deep inside the thin film. Besides that, the most interesting result is the magnetic property. As shown in Fig. 3(c), instead of having AFM coupling, the surface layer which contains an oxygen vacancy shows an FM coupling. This result is observed in the self-consistent calculations and also confirmed by the calculated exchange parameters. Combined

TABLE II. Calculated magnetocrystalline anisotropy energy for the SMO structures with and without oxygen vacancy. The MAE is computed by $E_{MAE} = E_{hard} - E_{easy}$, and the energy for the easy axis is set to zero. Unit in meV.

	[100]	[010]	[110]	[$\bar{1}$10]	[001]
Without vacancy	0.3	0.3	0.0	0.0	475.8
With vacancy	221.6	221.4	0.0	1371.6	84.0

with the increased magnitude of the moment on one of the Mn atoms (from 2.60 to 3.77 μ_B), the strength of this FM coupling is stronger than all the other couplings (18 meV compared to, for example,–4.35 meV from the second MnO_2 layer).

In addition to the changes in crystal structure and magnetic exchange parameters described in the main paper, the presence of an oxygen vacancy also affects the ground-state magnetic structure as well as the magnetocrystalline anisotropy energy of SMO. Results are shown in Tables I and II.

Furthermore, we found that the vacancy introduces significant distortions in the crystal structure. These distortions are evident in the changes to the B-O-B angles [see Fig. 3(b)]. Both in-plane (empty circles) and out-of-plane angles (empty triangles) have drastically different values compared to the structure without vacancy (filled circles and triangles). For the out-of-plane Mn-Mn pairs, there are two Mn chains along the z direction. These two chains perform differently in the structure with oxygen vacancy: they oscillate alternately, one after another. This interesting phenomenon is reflected in the out-of-plane exchange parameters. For the in-plane Mn-Mn pairs, the symmetry of the structure is reduced due to the distortion. Therefore the equivalent Mn-O-Mn angles in the structure without vacancy no longer exist. The behavior of corresponding J_{ij}s can be explained by the GKA rule: the bigger the deviation angle from 180°, the weaker the AFM coupling.

To detect the magnetic ordering in strained SMO thin films, spin Hall magnetoresistance measurements are performed. SMR is an established method to probe surface magnetic order and for extracting useful parameters such as magnetic anisotropy and spin mixing conductance in ferromagnetic [31,32], antiferromagnetic [33,34], and chiral magnetic insulators [35,36]. In SMR, spin Hall effect (SHE) mediated spin accumulation at the interface of a heavy metal, typically Platinum (Pt), and an insulating magnetic material is reflected or absorbed based on the orientation of surface magnetic moments. Upon applying a rotating external magnetic field, the magnetic order in SMO is manipulated, resulting in angular dependent magnetoresistance (ADMR) in Pt [31,37]. In this work, 8-nm-thick Pt nanostructures (0.5 × 7 μm) are fabricated on the SMO thin films using electron beam lithography and DC sputtering. The temperature-dependent Pt resistivity

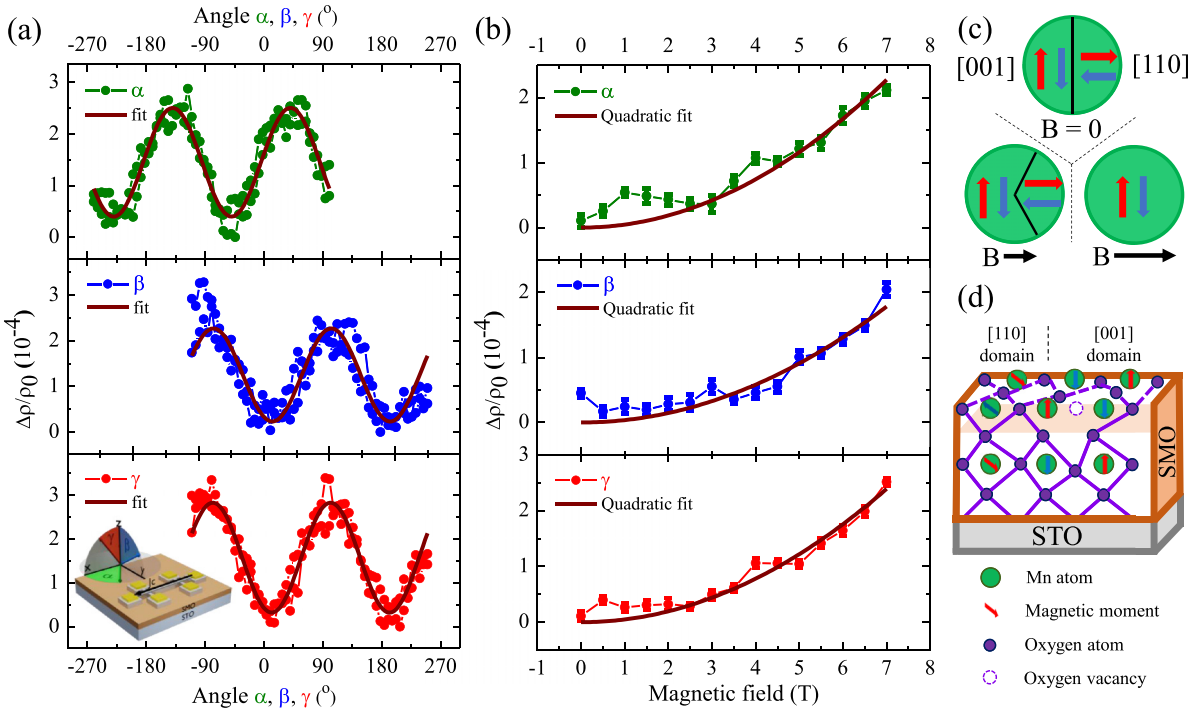

FIG. 4. In the top panel of (a), a 135-degree phase-shifted SMR curve is displayed for the α rotation, taken at 5 K using an external magnetic field of 7 T. The SMR in β and γ in the middle and bottom panels respectively both display a low resistance for out-of-plane angles. The curves are fitted with a $A * \sin^2(x\text{-}x_0) + y_0$ fit. In the γ panel inset, a schematic illustration of the sample and Pt Hall bar device, including definition of rotational directions, is shown. In (b) the magnitude of the field-dependent ADMR is shown for 5 K, which is fitted with a quadratic fit forced through the origin. The extracted quadratic coefficients for α, β, and γ are $4.6 \times 10^{-6} \pm 2.6 \times 10^{-7}$, $3.6 \times 10^{-6} \pm 2.3 \times 10^{-7}$, and $4.9 \times 10^{-6} \pm 2.0 \times 10^{-7}$, respectively. Panel (c) depicts the redistribution of antiferromagnetic domains by increasing the strength of an externally applied magnetic field. In (d), a sketch of the magnetic order in SMO thin films is shown, incorporating the domain types with anisotropy directions.

is shown in Fig. S4 [38]. An AC charge current J_c of 300 μA is applied in $\vec{x}$, corresponding to the [100] crystallographic direction as shown in Fig. 4(a) (inset, bottom panel). The generated spin accumulation in $\vec{y}$ is reflected or absorbed based on the orientation of the underlying magnetic moments, resulting in a charge voltage via the inverse spin Hall effect. This is measured as a resistance modulation in Pt for antiferromagnetic materials governed by the Néel vector $\vec{l}$ as [39–41]

$$\rho_{long} = \rho_0 + \tfrac{1}{2}\rho_1\left[1 - l_y^2\right], \tag{1}$$

where ρ_0 is the intrinsic Pt resistivity and ρ_1 a SMR coefficient based on SHE related parameters such as the spin Hall angle and spin mixing conductance [31]. The Néel vector is given by the difference of sublattice magnetic moments m as $\vec{l} = (\vec{m}_1 - \vec{m}_2)/2$. For applied fields strong enough to overcome the magnetic anisotropy, $\vec{l}$ orders perpendicular to the applied field direction, allowing canting towards the magnetic field to decrease Zeeman energy. This results in a negative SMR $[\sin^2(\alpha)]$ for AFMs with respect to positive SMR $[-\sin^2(\alpha)]$ in FMs [33,34] and with a phase shift of 90°. SMR measurements are performed for applied fields between 0 and 7 T at 5 K and for temperatures between 5 and 300 K at a constant field of 7 T. The obtained ADMR curves, shown in Fig. 4(a), are fitted with a sinusoidal dependence $[A\sin^2(x - x_0)]$ to extract the SMR magnitude (A) and phase (x_0). Remarkably, at 5 K a phase shift of 135° is observed in the α direction that cannot be explained by both AFM and FM SMR, as shown in Fig. 4(a). The obtained ADMR responses in β and γ directions are strikingly similar and are not consistent with SMR for either ferromagnets or antiferromagnets that are soft enough for the magnetic order vector to follow the applied magnetic field. However, considerations of a nontrivial preferred direction of the magnetic anisotropy can explain our findings.

By performing fully relativistic simulations, we find the magnetic easy axis to be along the [110] direction for both structures. The results are shown in Table S2. For the structure without oxygen vacancy, [–110] is an easy axis by symmetry of the tetragonal structure, and the [001] direction is a hard axis with an anisotropy energy of 475.8 meV, with the two in-plane orientations, [100] and [010], being equivalent with an anisotropy energy of 0.3 meV. Interestingly, our results for the structure with oxygen vacancy show that the [100] energy is increased to an energy of 222 meV, while the out-of-plane energy is reduced significantly to an energy of 84 meV. Due to the breaking of inversion symmetry, [–110] becomes a hard axis with an energy of 1372 meV such that [110] and [001] become the easiest anisotropy axes.

We assess other contributions, such as those arising from Hanle magnetoresistance (HMR) and weak antilocalization (WAL) to our data. A sizable contribution from HMR at low temperature is excluded, as this would result in a a 90° phase shift in β, which is not the case. WAL, though known to contribute in β and γ directions in Pt [32,42] due to the strong spin-orbit coupling at temperatures below 50 K, is not a dominant contributor in our case, as the out-of-plane direction has a low resistance with respect to the in-plane direction, which shows a higher resistance.

The quadratic dependence of SMR is unusual and compels us to consider the spatial orientation and distribution of antiferromagnetic domains in SMO with magnetic field. Here we propose a model where we consider that the spatial distribution of antiferromagnetic domains along [110] and [001] are manipulated by the external magnetic field. The choice for the anisotropy directions follows from the DFT calculations that predict a magnetic easy axis in the [110] direction and relatively low anisotropy energy in the [001] direction for oxygen-deficient SMO. Due to magnetic dipolar field energy, domains are expected to form in all magnetic materials, which affects the orientation of magnetic moments. Incorporating a domain fraction in Eq. (1) gives [40]

$$\rho_{long} = \rho_0 + \rho_1 \sum_k \xi_k\left[1 - \left(l_y^k\right)^2\right], \tag{2}$$

where ξ_k is the fraction of the magnetic domain k. The sum of the domain fractions should equal 1. A general expression of the fraction of the possible domains is given as

$$\xi_k = \xi_0\left[1 + \frac{2H^2}{H_{MD}^2} f(l_k, \delta)\right]. \tag{3}$$

Here H is the applied magnetic field, and H_{MD} is the magnetic field required to set a monodomain state in the magnetic volume [40]. Assuming both domain types are energetically degenerate, each occupies an equal volume in the absence of an applied field, described with $\xi_0 = 1\ /number\ of\ domains$. The function $f(l_k, \delta)$ is dependent on the relative direction between an applied magnetic field and the Néel vector of the particular domain, see Fig. S3c [38]. It governs the modulation of the resistance with the applied magnetic field such that the fraction of a domain is promoted when the Néel vector is perpendicular to the applied magnetic field. The field-induced Zeeman energy is then reduced by canting of the magnetic moments towards the applied magnetic field. A parallel alignment between the field and the Néel vector, on the other hand, is unfavorable, resulting in a reduction of these domains. Consequently, an applied magnetic field will change the domain fraction within the fixed magnetic volume.

Two possible domains are considered, where the Néel vector is in-plane, parallel to [110] ($k = 1$), and out-of-plane, parallel to [001] ($k = 2$), as indicated in Fig. S3 [38]. The SMR variation is obtained from the domain fractions (ξ_k) and the Néel vector projection onto $\vec{y}$ (l_y^k) for both domain types. This model assumes magnetic anisotropy is strong enough to have negligible spin canting such that when the field is applied perpendicular to the $(\bar{1}10)$ plane, the domain fractions are not affected. Hence the effective strength of the applied magnetic field is described by its projection onto the $(\bar{1}10)$ plane for the α, β, and γ rotations [41]. The resulting domain fractions and projected Néel vector are calculated as

$$\xi_1 = a\left[1 + \frac{2H^2}{H_{MD}^2}\cos(2\delta)\right] \quad l_y^1 = \frac{1}{\sqrt{2}} \tag{4}$$

and

$$\xi_2 = (1 - a)\left[1 + \frac{2H^2}{H_{MD}^2}\cos(2\delta - \pi)\right] \quad l_y^2 = 0, \tag{5}$$

where a ($0 \leqslant a \leqslant 1$) is the fraction of ξ_1 without an applied field. δ is defined as the angle between the [001] direction and the projection of the magnetic field onto the ($\bar{1}10$) plane, see Fig. S3c [38]. First we consider the rotation of the magnetic field in the α direction. By substituting the magnitude of the field, $|H_{(\bar{1}10)}(\alpha)|$, and the angle between the applied field vector and the ($\bar{1}10$) plane in Eqs. (4) and (5) and consequently in Eq. (2), we obtain the resistivity dependence for rotations in α as

$$\rho_{long}(\alpha) = \rho_0 + \rho_1\left[\left(1 - \frac{1}{2}a\right) + \left(1 - \frac{3}{2}a\right) \times \frac{2H^2}{H_{MD}^2}\cos^2\left(\frac{1}{4}\pi - \alpha\right)\right]. \quad (6)$$

Similarly, for rotations in β, the magnetic field magnitude and projection substituted yield the following for the domain fractions:

$$\xi_1(\beta) = a\left[1 + \frac{2H^2}{H_{MD}^2}\left(\cos^2(\beta) - \frac{1}{2}\sin^2(\beta)\right)\right], \quad (7)$$

$$\xi_2(\beta) = (1-a)\left[1 + \frac{2H^2}{H_{MD}^2}\left(-\cos^2(\beta) + \frac{1}{2}\sin^2(\beta)\right)\right]. \quad (8)$$

By symmetry, rotations in β and γ are equal and hence the resistivity for both can be written as

$$\rho_{long}(\beta,\gamma) = \rho_0 + \rho_1\left[\left(1 - \frac{1}{2}a\right) + \left(\frac{3}{2}a - 1\right)\frac{2H^2}{H_{MD}^2} + \left(\frac{3}{2} - \frac{9}{4}a\right)\frac{2H^2}{H_{MD}^2}\cos^2(\beta,\gamma)\right]. \quad (9)$$

To determine a, the parameter H_{MD} has to be known in addition to the SMR magnitudes of α and one out-of-plane rotational variation due to the interdependence of the rotational directions. However, the magnitudes of the oscillations are possibly impacted by other effects besides SMR, such as WAL and HMR. Given that the H_{MD} is not reached using an applied field of 7 T as no saturation of the SMR amplitude is observed, a is not determined. Therefore we assume that both contribute equally ($a = 1/2$). This reduces Eqs. (6) and (9) to

$$\rho_{long}(\alpha) = \rho_0 + \frac{3\rho_1}{4}\left[1 + \frac{2H^2}{3H_{MD}^2}\cos^2\left(\frac{1}{4}\pi - \alpha\right)\right] \quad (10)$$

and

$$\rho_{long}(\beta,\gamma) = \rho_0 + \frac{3\rho_1}{4}\left[1 - \frac{2H^2}{3H_{MD}^2} + \frac{H^2}{H_{MD}^2}\sin^2(\beta,\gamma)\right], \quad (11)$$

respectively.

The resulting phase obtained from the model for the three rotational variations matches the phase as measured by ADMR. As also evident from (10) and (11), the magnitude of the SMR in α should be smaller than for β and γ, which is not the case in experiments, see Fig. 4(b). This can occur due to either a difference between the anisotropy energies along [110] and [001] or non-negligible contributions from HMR and WAL.

Interestingly, we find a gradual decrease of the phase shift in SMR as the temperature increases from 5 to 300 K (left panel of Fig. 5). In the right panel the magnitude and phase extracted from the sinusoidal fits shows two distinct temperature regimes, indicated by the dashed lines at 100 K. Beyond 150 K, the finite magnitude and phase of 90° of the SMR signal in α and β, in addition to the diminishing SMR signal in γ, indicates that the magnetic ordering in SMO is lost. The disappearance of the SMR between 100 and 150 K is in fair agreement with the calculated SMO ordering temperatures from the DFT-based simulations [as shown in the inset of Fig. 3(c), the magnetic transition temperatures for stoichiometric and oxygen-deficient SMO are 143 and 121 K, respectively]. The gradual phase shift observed in all rotational directions is remarkable and suggests a modulation of the effective magnetic anisotropy with increasing temperature. Suppression of specific anisotropy axes may arise due to possible temperature-dependent structural properties such as polar order or strain similar to that reported in strained manganites such as $La_{0.67}Sr_0.67MnO_3$, where a strong temperature dependence of the magnetocrystalline anisotropy is observed [43,44].

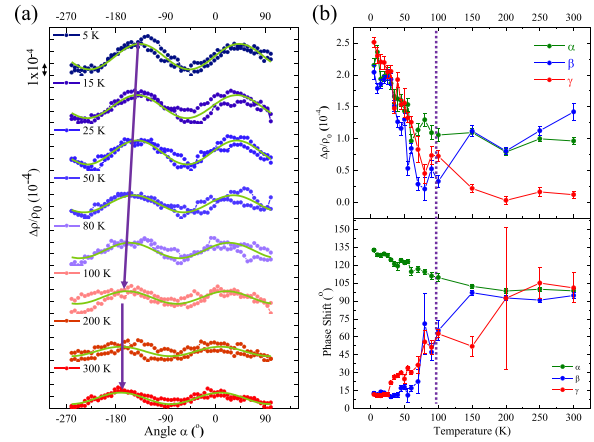

FIG. 5. The temperature-dependent SMR at 7 T for α in (a) indicates a gradual decrease of the phase shift up to 100 K, as indicated with the purple arrows. The phase shift and magnitude are extracted by fitting the resistance modulation with $A\ \sin^2(\alpha - x_0)$ (green line). In (b) the extracted temperature-dependent SMR magnitude and phase shift are displayed in the top and bottom panel, respectively, for all rotations. The error bars represent the fit error. Since there is no sizable signal for the γ phase at 200 K, a remarkable large fit error is obtained.

V. CONCLUSIONS

In conclusion, the antiferromagnetic character of strained SMO is revealed by phase-shifted spin Hall magnetoresistance in three rotational directions and explained by a model based on magnetic anisotropy and spatial redistribution of antiferromagnetic domains with the external field. Temperature-dependent SMR phase and magnitude affirms the gradual decrease of the magnetic anisotropy upon increasing temperature. The magnetic anisotropy in [110] and [001] directions, corroborated by DFT calculations, is consistent with the ferroelectric polarization direction predicted for strained SMO. A detailed analysis of interface and surface-induced structural distortions and correspond-

ing modifications of exchange interactions obtained from DFT+U calculations has been provided. Also, it has been shown that an O vacancy at the surface of the film introduces a ferromagnetic order at the surface layer. The results obtained from this work constitute an important step towards a comprehensive understanding of the magnetic order in strained SMO films, which is crucial for the development of antiferromagnetic spintronics, orbitronics, as well as for electric field control of magnetic order in multiferroic materials for alternative computing applications.

ACKNOWLEDGMENTS

J.J.L.vR. acknowledges financial support from a Dieptestrategie grant (2019), Zernike Institute for Advanced Materials. J.J.L.vR. and T.B. acknowledge technical support from J. Baas, J. G. Holstein, and H. H. de Vries and acknowledge A. Das, S. Chen, A. S. Goossens, M. A. Frantiu, G. E. W. Bauer and B. J. van Wees for useful discussions. This work was realized using NanoLab-NL facilities. The computations were enabled in Project SNIC 2021/3-38 by resources provided to B.S. by the Swedish National Infrastructure for Computing (SNIC) at NSC, PDC, and HPC2N partially funded by the Swedish Research Council through Grant Agreement No. 2018-05973. B.S. also acknowledges an allocation of supercomputing hours by the PRACE DECI-17 project Q2Dtopomat. D.W. acknowledges the China Scholarship Council for financial support (Grant No. 201706210084).

[1] S. Manipatruni, D. E. Nikonov, C. C. Lin, T. A. Gosavi, H. Liu, B. Prasad, Y. L. Huang, E. Bonturim, R. Ramesh, and I. A. Young, Nature (London) **565**, 35 (2019).
[2] N. A. Spaldin and R. Ramesh, Nat. Mater. **18**, 203 (2019).
[3] D. C. Vaz, C.-C. Lin, J. Plombon, W. Y. Choi, I. Groen, I. Arango, V. T. Pham, D. E. Nikonov, H. Li, P. Debashis, S. B. Clendenning, T. A. Gosavi, V. Garcia, S. Fusil, M. Bibes, Y.-L. Huang, B. Prasad, R. Ramesh, F. Casanova, and I. A. Young, Functional demonstration of a fully integrated magneto-electric spin-orbit device, in *2021 IEEE International Electron Devices Meeting (IEDM)* (IEEE, 2021), pp. 32.4.1–32.4.4.
[4] A. Edström and C. Ederer, Phys. Rev. Lett. **124**, 167201 (2020).
[5] A. Edström and C. Ederer, Phys. Rev. Mater. **2**, 104409 (2018).
[6] J. H. Lee and K. M. Rabe, Phys. Rev. Lett. **104**, 207204 (2010).
[7] X. Zhu, A. Edström, and C. Ederer, Phys. Rev. B **101**, 064401 (2020).
[8] R. Guzmán, L. Maurel, E. Langenberg, A. R. Lupini, P. A. Algarabel, J. A. Pardo, and C. Magén, Nano Lett. **16**, 2221 (2016).
[9] J. Schaab, I. P. Krug, H. Doanay, J. Hackl, D. M. Gottlob, M. I. Khan, S. Nemšák, L. Maurel, E. Langenberg, P. A. Algarabel, J. A. Pardo, C. M. Schneider, and D. Meier, Phys. Rev. Appl. **5**, 054009 (2016).
[10] C. Becher, L. Maurel, U. Aschauer, M. Lilienblum, C. Magén, D. Meier, E. Langenberg, M. Trassin, J. Blasco, I. P. Krug, P. A. Algarabel, N. A. Spaldin, J. A. Pardo, and M. Fiebig, Nat. Nanotechnol. **10**, 661 (2015).
[11] J. W. Guo, P. S. Wang, Y. Yuan, Q. He, J. L. Lu, T. Z. Chen, S. Z. Yang, Y. J. Wang, R. Erni, M. D. Rossell, V. Gopalan, H. J. Xiang, Y. Tokura, and P. Yu, Phys. Rev. B **97**, 235135 (2018).
[12] H. An, Y. G. Choi, Y. R. Jo, H. J. Hong, J. K. Kim, O. Kwon, S. Kim, M. Son, J. Yang, J. C. Park, H. Choi, J. Lee, J. Song, M. H. Ham, S. Ryu, Y. Kim, C. W. Bark, K. T. Ko, B. J. Kim, and S. Lee, NPG Asia Mater. **13**, 69(2021).
[13] H. Wang, X. Jiang, Y. Wang, R. W. Stark, P. A. Van Aken, J. Mannhart, and H. Boschker, Nano Lett. **20**, 88 (2020).
[14] E. Langenberg, L. Maurel, G. Antorrena, P. A. Algarabel, C. Magén, and J. A. Pardo, ACS Omega **6**, 13144 (2021).
[15] M. Kaviani and U. Aschauer, Phys. Chem. Chem. Phys. **24**, 3951 (2022).
[16] F. Wang, Y. Q. Zhang, Y. Bai, W. Liu, H. R. Zhang, W. Y. Wang, S. K. Li, S. Ma, X. G. Zhao, J. R. Sun, Z. H. Wang, Z. J. Wang, and Z. D. Zhang, Appl. Phys. Lett. **109**, 052403 (2016).
[17] P. Agrawal, J. Guo, P. Yu, C. Hébert, D. Passerone, R. Erni, and M. D. Rossell, Phys. Rev. B **94**, 104101 (2016).
[18] A. Das, V. E. Phanindra, A. J. Watson, and T. Banerjee, Appl. Phys. Lett. **118**, 052407 (2021).
[19] G. Koster, B. L. Kropman, G. J. Rijnders, D. H. Blank, and H. Rogalla, Appl. Phys. Lett. **73**, 2920 (1998).
[20] P. E. Blöchl, Phys. Rev. B **50**, 17953 (1994).
[21] G. Kresse and D. Joubert, Phys. Rev. B **59**, 1758 (1999).
[22] G. Kresse and J. Furthmüller, Comput. Mater. Sci. **6**, 15 (1996).
[23] A. I. Liechtenstein, M. I. Katsnelson, V. P. Antropov, and V. A. Gubanov, J. Magn. Magn. Mater. **67**, 65 (1987).
[24] J. M. Wills, M. Alouani, P. Andersson, A. Delin, O. Eriksson, and O. Grechnyev, *Full-Potential Electronic Structure Method: Energy and Force Calculations with Density Functional and Dynamical Mean Field Theory* (Springer Science & Business Media, New York, 2010), Vol. 167.
[25] J. P. Perdew, K. Burke, and M. Ernzerhof, Phys. Rev. Lett. **77**, 3865 (1996).
[26] V. I. Anisimov, F. Aryasetiawan, and A. I. Lichtenstein, J. Phys.: Condens. Matter **9**, 767 (1997).
[27] S. L. Dudarev, G. A. Botton, S. Y. Savrasov, C. J. Humphreys, and A. P. Sutton, Phys. Rev. B **57**, 1505 (1998).
[28] O. Eriksson, A. Bergman, L. Bergqvist, and J. Hellsvik, *Atomistic Spin Dynamics: Foundations and Applications* (Oxford University Press, Oxford, England, 2017).
[29] G. Henkelman, B. P. Uberuaga, and H. Jónsson, J. Chem. Phys. **113**, 9901 (2000).
[30] G. Henkelman and H. Jónsson, J. Chem. Phys. **113**, 9978 (2000).
[31] N. Vlietstra, J. Shan, V. Castel, B. J. Van Wees, and J. Ben Youssef, Phys. Rev. B **87**, 184421 (2013).
[32] S. Vélez, V. N. Golovach, A. Bedoya-Pinto, M. Isasa, E. Sagasta, M. Abadia, C. Rogero, L. E. Hueso, F. S. Bergeret, and F. Casanova, Phys. Rev. Lett. **116**, 016603 (2016).

[33] G. R. Hoogeboom, A. Aqeel, T. Kuschel, T. T. Palstra, and B. J. Van Wees, Appl. Phys. Lett. **111**, 052409 (2017).

[34] R. Lebrun, A. Ross, O. Gomonay, S. A. Bender, L. Baldrati, F. Kronast, A. Qaiumzadeh, J. Sinova, A. Brataas, R. A. Duine, and M. Kläui, Commun. Phys. **2**, 50 (2019).

[35] A. Aqeel, M. Azhar, N. Vlietstra, A. Pozzi, J. Sahliger, H. Huebl, T. T. Palstra, C. H. Back, and M. Mostovoy, Phys. Rev. B **103**, L100410 (2021).

[36] A. Aqeel, N. Vlietstra, J. A. Heuver, G. E. Bauer, B. Noheda, B. J. Van Wees, and T. T. Palstra, Phys. Rev. B **92**, 224410 (2015).

[37] K.-i. Uchida, J. Xiao, H. Adachi, J.-i. Ohe, S. Takahashi, J. Ieda, T. Ota, Y. Kajiwara, H. Umezawa, H. Kawai, *et al.*, Nat. Mater. **9**, 894 (2010).

[38] See Supplemental Material at http://link.aps.org/supplemental/10.1103/PhysRevB.106.214415 for growth characteristics and surface topography, second harmonic response, high temperature ADMR, and spin hall magnetoresistance model based on anisotropy and domain formation.

[39] Y. T. Chen, S. Takahashi, H. Nakayama, M. Althammer, S. T. B. Goennenwein, E. Saitoh, and G. E. W. Bauer, Phys. Rev. B **87**, 144411 (2013).

[40] J. Fischer, O. Gomonay, R. Schlitz, K. Ganzhorn, N. Vlietstra, M. Althammer, H. Huebl, M. Opel, R. Gross, S. T. B. Goennenwein, and S. Geprägs, Phys. Rev. B **97**, 014417 (2018).

[41] S. Geprägs, M. Opel, J. Fischer, O. Gomonay, P. Schwenke, M. Althammer, H. Huebl, and R. Gross, J. Appl. Phys. **127**, 243902 (2020).

[42] V. E. Phanindra, A. Das, J. J. L. van Rijn, S. Chen, B. J. van Wees, and T. Banerjee, arXiv:2201.08685.

[43] A. A. Burema and T. Banerjee, Appl. Phys. Lett. **119**, 011901 (2021).

[44] A. A. Burema, J. J. van Rijn, and T. Banerjee, J. Magn. Magn. Mater. **549**, 168910 (2022).